A Novel Detail-Enhancement Method for Industrial Digital Radiography via Gaussian-Free Multiscale Laplacian Adaptive Fusion

Guancheng Lu, Zhen Dong, Jin Wei, Guiqing Li, Jihua Guan & Wei Wei

Guangxi University

ABSTRACT

This study introduces a concise framework for detail enhancement in industrial digital radiography based on the mathematical integration of logarithmic transformation and multiscale Laplacian analysis. The proposed method utilizes multiscale adaptive pixel-level fusion with hyperbolic tangent-based coefficients to preserve microscale defects while enhancing subtle features throughout the dynamic range. Quantitative evaluations of diverse industrial welds, including ship plates, boilers, and oil pipelines, demonstrated substantial improvements. In oil pipeline weld inspections, the Peak Signal-to-Noise Ratio of the method based on Histogram Equalization increased by 133.82%, whereas the Structural Similarity Index Measure and Spatial Frequency metrics exhibited gains of up to 127.27% and 85.81%, respectively. The framework's consistent, albeit moderate, performance gains over state-of-the-art deep learning methods across all benchmarks confirm its value not only as a robust and widely applicable tool but also as a superior preprocessing or integrated solution within nondestructive testing pipelines.

Keywords: digital radiography, multiscale analysis, pixel-level fusion, image detail enhancement, nondestructive testing.

Classification: FoR Code: 460205

Language: English

Great Britain Journals Press

LJP Copyright ID: 392953
Print ISSN: 2631-8474
Online ISSN: 2631-8482

London Journal of Engineering Research

Volume 25 | Issue 5 | Compilation 1.0

A Novel Detail-Enhancement Method for Industrial Digital Radiography via Gaussian-Free Multiscale Laplacian Adaptive Fusion

Guancheng Lu[α], Zhen Dong[σ], Jin Wei[ρ], Guiqing Li[ↀ], Jihua Guan[¥] & Wei Wei[§]

ABSTRACT

This study introduces a concise framework for detail enhancement in industrial digital radiography based on the mathematical integration of logarithmic transformation and multiscale Laplacian analysis. The proposed method utilizes multiscale adaptive pixel-level fusion with hyperbolic tangent-based coefficients to preserve microscale defects while enhancing subtle features throughout the dynamic range. Quantitative evaluations of diverse industrial welds, including ship plates, boilers, and oil pipelines, demonstrated substantial improvements. In oil pipeline weld inspections, the Peak Signal-to-Noise Ratio of the method based on Histogram Equalization increased by 133.82%, whereas the Structural Similarity Index Measure and Spatial Frequency metrics exhibited gains of up to 127.27% and 85.81%, respectively. The framework's consistent, albeit moderate, performance gains over state-of-the-art deep learning methods across all benchmarks confirm its value not only as a robust and widely applicable tool but also as a superior preprocessing or integrated solution within nondestructive testing pipelines.

Keywords: digital radiography, multiscale analysis, pixel-level fusion, image detail enhancement, nondestructive testing.

Author α σ ρ §: School of Mechanical Engineering, Guangxi University, Nanning 530004, China.
ↀ ¥: Guangxi Laboratory of Forestry, Guangxi Forestry Research Institute, Nanning 530002, China.

Table 1: List of Notations and Symbols

Symbol	Comment
a	Logarithm base
c	Center position index of Laplacian kernel
d	Manhattan distance from the center
$f(x,y)$	Continuous image intensity function at spatial coordinates (x,y)
f_c	Cutoff frequency in cycles per pixel
$F_{final}(x,y)$	Final fusion result of the pixel at coordinates (x,y)
f_k	A proportionality constant typically ranging from 0.6 to 0.8
$F_k(x,y)$	Enhanced image at scale k
F_{min}	Minimum value of the fusion result across the entire image
F_{max}	Maximum value of the fusion result across the entire image
$G(i,j,\sigma)$	Value of Gaussian kernel at scale σ and position (i,j)
H	Image height
$H(x,y)$	Mean curvature of the intensity surface at pixel (x,y)
$H_G(E)$	Horizontal gradient of the image E between the adjacent pixels in the same row
$I(x,y)$	Discrete image intensity at pixel coordinates (x,y)
$I_{enhanced}(x,y)$	Enhanced image pixel value in grayscale levels at position (x,y)
$I_{log}(x,y)$	Pixel value at position (x,y) after the logarithmic transformation
$I_{orig}(x,y)$	Original pixel value at position (x,y)
$I_{smooth}(x,y,\sigma)$	Smoothed image at scale σ and position (x,y)

Symbol	Comment
$K_{3\times3}$	A standard 3×3 discrete Laplacian kernel
$K_{5\times5}(i,j)$	Value of the 5×5 Laplacian kernel at position (i,j)
$K_{\text{Laplace},k}$	Laplacian kernel of size $(3+2k)\times(3+2k)$ at scale k
$L(x,y)$	Discrete Laplacian response at position (x,y)
N	Total number of scales
$PSNR(E,S)$	Peak signal-to-noise ratio of image E relative to image S
round(·)	Rounding function to the nearest integer
$R_{\text{base}}(x,y)$	Benchmark for Laplacian response differential analysis that is initialized with zeros and becomes the convolution result of the minimal Laplacian kernel once the Laplacian operation is performed.
$R_k(x,y)$	Laplacian response at scale k and position (x,y), which uses the kth Laplacian kernel to convolve the image
size	Laplacian kernel size
$SF(E)$	Spatial frequency of image E
$SSIM(E,S)$	Structural similarity index measure of the image E relative to the image S
tanh (·)	Hyperbolic tangent function
$V_{\text{grayscale}}$	Grayscale value of DR image
$V_G(E)$	Compute the vertical gradient of the image E
V_{display}	Display value
W	Image width
WL	Window level
WW	Window width
$\nabla^2 f(x,y)$	Laplacian operator at spatial coordinates (x,y)
$\partial^2 f(x,y)/\partial x^2$	Second-order partial derivatives in the respective spatial direction X
$\partial^2 f(x,y)/\partial y^2$	Second-order partial derivatives in the respective spatial direction Y
$\nabla^2 G(x,y)$	the Laplacian of the intensity function at pixel (x,y)
$\nabla G(x,y)$	the gradient vector field at pixel (x,y)
$\lvert\nabla G(x,y)\rvert$	the magnitude of the gradient vector at pixel (x,y)
*	Convolution operation
$\lvert\nabla^2 R(x,y)\rvert$	Magnitude of the Laplacian response at pixel coordinates (x,y)
$\mathrm{d}^2R(x,y)/\mathrm{d}s^2$	Second directional derivative along the gradient direction
$\Delta_k(x,y)$	Differences in details between scale k and the benchmark for Laplacian response
a	Logarithm base
δ	A small offset to avoid mathematical singularity at zero
$\mathrm{d}I\log(x,y)/\mathrm{d}I_{\text{orig}}(x,y)$	Derivative of the logarithmic transformation at position (x,y)
$\alpha_k(x,y)$	Importance coefficient of the pixel at position (x,y) and scale k
λ	A factor that controls the detail enhancement sensitivity
$F\{\cdot\}$	Fourier transform operator
(u,v)	Spatial frequency coordinates

I. INTRODUCTION

Industrial digital radiography (DR) has emerged as a critical technology for nondestructive evaluation in precision manufacturing sectors, including the aerospace, automotive, and nuclear power industries[1-3]. DR images characterized by pixel values spanning 0 to 65535 provide an extensive dynamic range for capturing subtle material variations while simultaneously presenting significant challenges for defect detection and characterization[3, 4]. Conventional image enhancement techniques often encounter difficulties in balancing the competing requirements of noise suppression and detail preservation, particularly when addressing micron-scale defects that manifest as minimal intensity variations within complex industrial components[5-7].

The current landscape of industrial DR image enhancement reveals fundamental limitations in

several methodological approaches[3, 8, 9]. Gaussian-dependent multiscale analysis, while effective for noise reduction, intrinsically compromises fine structural details through the systematic attenuation of high-frequency components that are essential for defect characterization[3, 10]. Methods based on discrete wavelet transform (DWT) encounter challenges in optimal basis selection and often introduce reconstruction artifacts when processing complex defect morphologies[11-13]. Histogram equalization (HE) and contrast-limited adaptive histogram equalization (CLAHE) techniques, despite their computational simplicity, frequently produce unnatural contrast amplification and fail to preserve subtle intensity gradients that are critical for accurate defect assessment[14-16]. Although deep learning (DL) approaches, such as methods based on convolutional neural network (CNN), are promising in certain domains, they face substantial limitations, including extensive data requirements, limited interpretability, poor generalization across diverse industrial scenarios, and a lack of physical interpretability[9, 10, 17, 18]. Furthermore, these methods collectively exhibit significant computational complexity, and their parameter sensitivity necessitates extensive manual optimization, undermining operational efficiency in industrial environments[3, 10, 19, 20]. These multifaceted challenges underscore the critical need for a fundamentally new paradigm that can simultaneously address the competing demands of computational efficiency, physical interpretability, and uncompromised detail preservation[6, 21, 22].

To address these challenges, this study introduces a paradigm-shifting framework characterized by a Gaussian-free architecture and pixel-level fusion technology. The proposed method establishes a novel integration of perceptually aligned logarithmic transformation with direct multiscale Laplacian analysis, achieving unprecedented detail preservation while maintaining computational tractability. The framework incorporates an adaptive fusion mechanism governed by hyperbolic tangent importance coefficients, enabling the selective enhancement of defect regions while preserving structural integrity through physically interpretable operations. This approach ensures complete mathematical transparency and eliminates the black-box characteristics that impede the industrial adoption of many contemporary techniques. The principal contributions of this study encompass three key innovations: (1) a comprehensive Gaussian-free mathematical framework that fundamentally redefines multiscale enhancement while preserving computational efficiency; (2) an adaptive pixel-level fusion technology with precise control mechanisms for defect-specific enhancement; and (3) a rigorous theoretical foundation with complete mathematical derivations validated across diverse industrial applications. These advances collectively provide an engineering-friendly solution that balances the enhancement efficacy with the ease of implementation while maintaining full physical interpretability throughout the enhancement pipeline.

This paper is systematically organized to present a novel detail-enhancement method for industrial DR images using multiscale pixel-level fusion techniques. Section 2 establishes the theoretical foundation by reviewing the fundamental concepts of Laplacian transform theory, differential geometric interpretations, discrete implementations, logarithmic transformation principles, and industrial DR imaging characteristics. Section 3 introduces the proposed methodology in detail, beginning with the fundamental principles, followed by the mathematical formulation of the pixel-level adaptive fusion coefficient, construction of multiscale space using Laplacian convolution operator, multiscale pixel-level fusion methodology, enhanced image reconstruction procedures, and strategic avoidance of Gaussian-induced detail destruction. Section 4 presents the experimental setup and analytical methodologies employed for the validation. Section 5 discusses the experimental results and provides a comprehensive analysis of the method's performance, limitations, and potential improvements. Finally, Section 6 concludes the

paper by summarizing the key findings and outlining future research directions.

II. RELATED WORK

2.1 Laplacian Transform Theory

The Laplacian transform is a fundamental mathematical construct in image processing that serves as a second-order differential operator that characterizes local intensity variations through the divergence measurement of the gradient field[23-25]. The continuous two-dimensional equation expresses this relationship as follows:

$$\nabla^2 f(x,y) = \frac{\partial^2 f(x,y)}{\partial x^2} + \frac{\partial^2 f(x,y)}{\partial\ ^2}\# \quad (1)$$

$$\frac{\partial^2 I(x,y)}{\partial x^2} \approx I(x+1,y) - 2I(x,y) + I(x-1,y)\# \quad (2)$$

$$\frac{\partial^2 I(x,y)}{\partial y^2} \approx I(x,y+1) - 2I(x,y) + I(x,y-1)\# \quad (3)$$

where $I(x,y)$ represents the discrete image intensity at pixel coordinates (x,y), and $I(x+1,y)$, $I(x-1,y)$, $I(x,y+1)$, and $I(x,y-1)$ denote the intensity values at adjacent pixel positions. The composite discrete Laplacian operator combines these approximations as follows:

$$L(x,y) = I(x+1,y) + I(x-1,y) + I(x,y+1) + I(x,y-1) - 4I(x,y)\# \quad (4)$$

where $L(x,y)$ represents the discrete Laplacian response at position (x,y).

The Laplacian transform effectively computes the difference between each pixel and its local neighborhood average, functioning as a high-pass filter that amplifies regions with significant intensity variations and suppresses homogeneous areas. It captures the essence of the local curvature in intensity surfaces by quantifying how the average value of a function in the neighborhood of a point differs from its value at the point.

The geometric interpretation of the Laplacian operator reveals its profound connection to surface curvature characteristics [26, 27]. This relationship is formalized by the mean curvature equation:

$$H(x,y) = \frac{\nabla^2 G(x,y)}{2(1+|\nabla G(x,y)|^2)^{3/2}}\# \quad (5)$$

where $\nabla^2 f(x,y)$ denotes the Laplacian operator at spatial coordinates (x,y), $f(x,y)$ represents the continuous image intensity function at spatial coordinates (x,y), $\partial^2 f(x,y)/\partial x^2$ indicates the second-order partial derivatives in the respective spatial direction X, and $\partial^2 f(x,y)/\partial y^2$ indicates the second-order partial derivatives in the respective spatial direction Y.

The discrete implementation employs central difference approximations to achieve computational efficiency while maintaining the mathematical accuracy:

where $H(x,y)$ represents the mean curvature of the intensity surface at pixel (x,y), $\nabla^2 G(x,y)$ denotes the Laplacian of the intensity function at pixel (x,y), $\nabla G(x,y)$ represents the gradient vector field at pixel (x,y), and $|\nabla G(x,y)|$ indicates the magnitude of the gradient vector at pixel (x,y). This mathematical relationship demonstrates that Laplacian responses correlate directly with the local curvature of the intensity landscape, generating strong outputs in regions with high curvature, such as edges, corners, and fine details, while producing minimal responses in relatively flat homogeneous areas.

2.2 Logarithmic Transformation Theory

The logarithmic transformation addresses the fundamental challenge of a high dynamic range in industrial DR images through nonlinear mapping, which compresses the extensive intensity range while preserving the relative contrast

relationships. The mathematical equation defining this transformation is as follows:

$$I_{\log}(x,y) = \log_a(I_{\text{orig}}(x,y) + \delta) \quad (6)$$

where $I_{\text{orig}}(x, y)$ is the original pixel value at position (x, y), $I_{\log}(x, y)$ represents the pixel value at position (x, y) after the logarithmic transformation, a denotes the logarithm base, *and* δ provides a small offset to avoid mathematical singularity at zero.

The transformation employs a compressive nonlinearity to enhance contrast in dark regions and prevent saturation in bright areas, thereby directly addressing the challenge of defects distributed across the full intensity spectrum in industrial DR imaging[28, 29]. Furthermore, derivative analysis confirms that this process intrinsically converts multiplicative noise into an additive form. This critical transformation, which simplifies subsequent denoising while preserving structural integrity, is mathematically expressed as

$$\frac{dI_{\log}(x,y)}{dI_{\text{orig}(x,y)}} = \frac{1}{(I_{\text{orig}}(x,y) + \delta)\ln a} \quad (7)$$

where $dI\log(x,y)/dI_{\text{orig}}(x,y)$ represents the derivative of the logarithmic transformation at position (x,y), indicating the local gain applied during mapping.

$$V_{\text{display}} = \begin{cases} 0 & V_{\text{grayscale}} \le WL - \frac{WW}{2} \\ 255\,\frac{V_{\text{grayscale}} - (WL - \frac{WW}{2})}{WW} & WL - \frac{WW}{2} < V_{\text{grayscale}} < WL + \frac{WW}{2} \\ 255 & V_{\text{grayscale}} \ge WL + \frac{WW}{2} \end{cases} \quad (8)$$

where V_{display} is the display value, WL represents the window level that determines the dynamic range centered for display, and WW denotes the window width that controls the contrast by determining the width of the range of values mapped to the display range. This essential visualization technique enables inspectors to navigate the vast intensity space by dynamically adjusting the displayed contrast and brightness, effectively isolating regions of interest within the 16-bit data for detailed examination[20, 31].

By applying a high gain to the dark regions and a low gain to the bright regions, this derivative enables adaptive enhancement across the dynamic range, directly overcoming the limitations of the uniform linear gain. Moreover, the logarithmic operation renders the noise additive, allowing for its effective removal while protecting critical spatial details from the blurring effects of spatial smoothing. Together, these properties establish a robust method for reducing the influence of noise in DR-image-detail enhancement.

2.3 DR Image Display Principles

DR images are often stored in Digital Imaging and Communications in Medicine (DICOM) files with a 16-bit grayscale[4, 30]. The 16-bit grayscale depth of DR images far exceeds the 256 levels available in standard 8-bit displays. This fundamental disparity creates a critical visualization bottleneck that can obscure subtle defect signatures and material variations essential for an accurate nondestructive evaluation. Practical visualization of DR images employs window-level adjustments to accommodate conventional display systems using the following equation:

III. PROPOSED METHOD

3.1 Methodological Principles

Fig. 1 depicts the overall architecture of the proposed framework, which addresses the fundamental challenges of industrial DR image enhancement by integrating logarithmic transformation with a multiscale Laplacian analysis. The proposed framework is initiated with a logarithmic transformation of the input image to compress its dynamic range and

attenuate noise interference. A multiscale representation is then constructed by convolving the transformed image with Laplacian kernels of progressively increasing sizes, generating a series of response maps that capture the edge and detail information across distinct spatial frequencies. Subsequently, a pixel-importance coefficient map is derived at each scale by comparing its Laplacian response to a designated benchmark. These comparative measurements are processed through a nonlinear activation function to ensure numerical stability. The resulting coefficients subsequently orchestrate a pixel-level fusion process, wherein multiscale detail components are adaptively and proportionally integrated into the logarithmically transformed image. The procedure culminates in a reconstruction phase accompanied by dynamic range normalization, ultimately yielding an enhanced DR image with fused pixels.

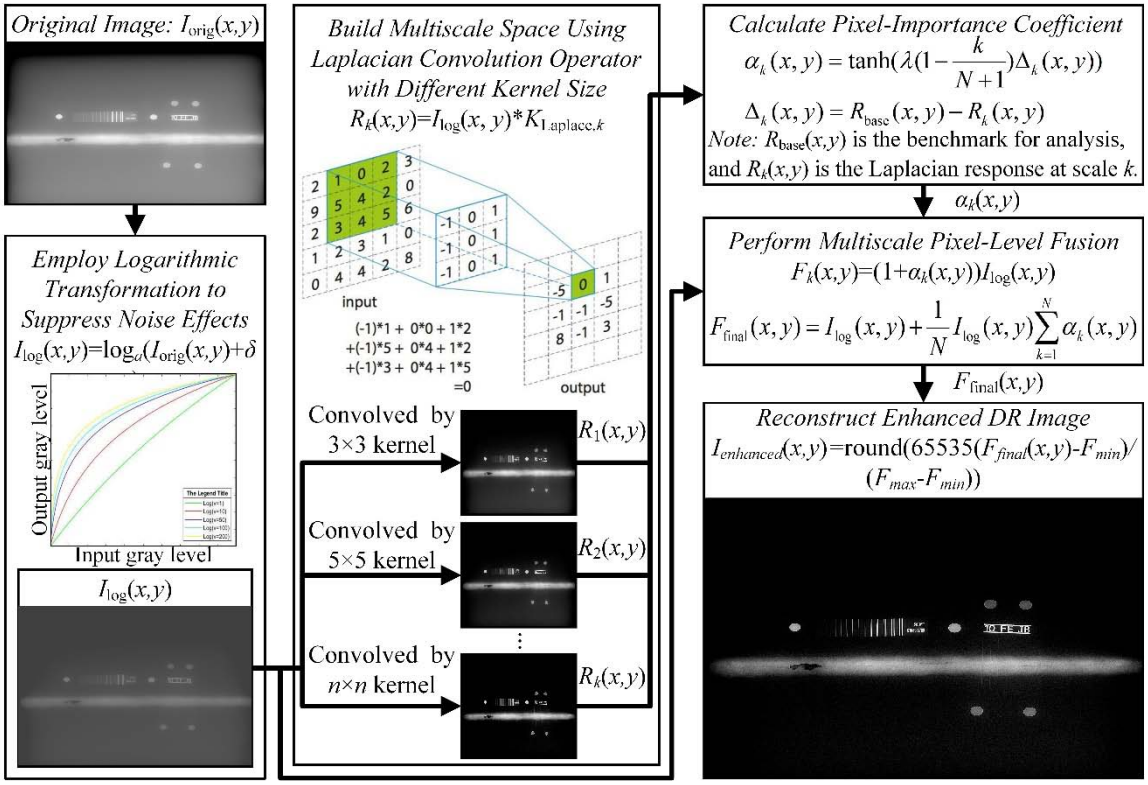

Fig. 1: Principle of Proposed Method

The key idea is to develop a mathematical formulation that entirely obviates Gaussian convolution while preserving the effective enhancement performance. The detail detection mechanism is derived from the fundamental relationship between the Laplacian response and the second-order directional derivative:

$$|\nabla^2 R(x,y)| \propto \left|\frac{\mathrm{d}^2 R(x,y)}{\mathrm{d}s^2}\right| \# \qquad (9)$$

where $|\nabla^2 R(x,y)|$ represents the magnitude of the Laplacian response at pixel coordinates (x,y), $\mathrm{d}^2R(x,y)/\mathrm{d}s^2$ denotes the second directional derivative along the gradient direction, and the proportionality indicates that the Laplacian magnitude corresponds directly to the acceleration of intensity change along the gradient directions, responding most strongly to locations where intensity transitions occur rapidly, such as at edges, corners, and fine texture patterns.

The Laplacian operator capitalizes on its second-order nature to identify fine defects in industrial DR images by highlighting localized intensity transitions. This enables a detailed enhancement scheme that performs pixel-level adaptive fusion using importance coefficients from multiscale Laplacian responses, as follows:

$$F_{\text{final}}(x,y) = \frac{1}{N}\sum_{k=1}^{N}(1+\alpha_k(x,y))\, I_{\log}(x,y) \qquad (10)$$

where $F_{final}(x,y)$ represents the final pixel-level fusion result at position (x,y), N denotes the total number of scales, and $\alpha_k(x,y)$ signifies the pixel-importance coefficient at position (x,y) and scale k. This formulation represents a sophisticated blending of multiscale information, in which the term $(1+\alpha_k(x,y))$ functions as an adaptive gain factor that varies spatially and across different scales. When $\alpha_k(x,y)$ assumes positive values, indicating the presence of significant details at scale k, the gain increases to enhance these details. Conversely, when $\alpha_k(x,y)$ takes negative values, suggesting the absence of meaningful details, the gain decreases to suppress the noise or irrelevant variations.

3.2 Method for Calculating Pixel-Level Adaptive Fusion Coefficient

The pixel-importance coefficient serves as the pixel-level adaptive fusion coefficient. It plays a pivotal role in determining the appropriate enhancement strength at each pixel location across different scales, with the calculation employing the hyperbolic tangent function for adaptive coefficient generation as follows:

$$\alpha_k(x,y) = \tanh(\lambda(1-\frac{k}{N+1})\Delta_k(x,y))\# \quad (11)$$

where $\tanh(\cdot)$ denotes the hyperbolic tangent function, $\Delta_k(x,y)$ represents the differences in details between scale k and the benchmark for the Laplacian response differential analysis at position (x,y), λ is a factor that controls the detail enhancement sensitivity because $\Delta_k(x,y)$ is often a small value, and the term $\lambda(1-k/(N+1))$ adaptively tunes $\Delta_k(x,y)$ based on the fact that the convolution result of a smaller Laplacian kernel contains more important information than a larger one. A higher λ enhances the contrast but loses some extremely fine features. Empirical evidence suggests that λ typically ranges from $3N$ to $7N$.

According to Laplace theory, larger Laplace kernels preserve global textures, whereas smaller Laplace kernels retain local details. Based on this principle, the physical implication of Equation (11) is that the greater the deviation of the convolutional responses using Laplace kernels of different sizes relative to the Laplacian response analytical baseline, the more detailed the information contained in the pixel, and the more critical it becomes for enhancing details.

In Equation (11), the hyperbolic tangent function serves as a smooth, bounded activation function that converts raw detail differences into normalized importance coefficients within the range (-1,1). The characteristic S-shaped curve of this function provides several advantageous properties: (1) for small detail differences, it operates in an approximately linear region, delivering a proportional response to subtle variations; (2) for large differences, it saturates to ±1, preventing over-enhancement that could introduce artificial artifacts or unnatural appearances. This saturation behavior is crucial for maintaining visually coherent results while providing a robust enhancement. The parameter λ controls the steepness of the transition between the linear and saturated regions, effectively determining the sensitivity to detail variations and allowing adjustment based on specific image characteristics and enhancement requirements.

Based on the principle of Laplacian response, the method for calculating the differences in details is as follows:

$$\Delta_k(x,y) = R_{\text{base}}(x,y) - R_k(x,y)\# \quad (12)$$

where $R_{base}(x,y)$ is the benchmark for the Laplacian response differential analysis, which is initialized with zeros and becomes the convolution result of the minimal Laplacian kernel once the Laplacian operation is performed, and $R_k(x,y)$ represents the Laplacian response at scale k and position (x,y), obtained by convolving the image with the kth Laplacian kernel.

Based on Equation (12), positive values of $\Delta_k(x,y)$ indicate that the finest-scale kernel detects details that are not captured by the larger kernel, suggesting the presence of fine-scale features such as small defects or sharp edges, whereas negative values of $\Delta_k(x,y)$ suggest that the larger kernel responds more strongly, indicating the presence of larger-scale structures or more gradual variations in the intensity. This multiscale difference approach effectively separates the

details of different spatial extents, enabling the targeted enhancement of specific feature sizes without affecting others and providing comprehensive coverage across the spectrum of defect scales present in DR images.

3.3 Method for Building Multiscale Space using Laplacian Convolution Operator

Multiscale analysis employs direct Laplacian kernels of varying sizes applied to the logarithmically transformed image, completely avoiding the Gaussian convolution operations that characterize traditional approaches.

$$R_k(x,y) = I_{\log}(x,y) * K_{\text{Laplace},k}, k = 1,2,\ldots,N\# \tag{13}$$

where $*$ denotes the convolution operation, and $K_{\text{Laplace},k}$ signifies the Laplacian kernel of size $(3+2k)\times(3+2k)$ at scale k. This multiscale methodology represents a fundamental departure from Gaussian-based methods by applying Laplacian kernels of different sizes directly to the image, thereby preserving the high-frequency information that would otherwise be attenuated by the Gaussian smoothing. Each kernel size responds preferentially to features of particular spatial extents: smaller kernels capture fine details and sharp edges, whereas larger kernels respond to broader structures and more gradual intensity variations. This comprehensive representation across feature scales is essential for detecting the diverse range of defects encountered in industrial DR applications.

The kernel design follows a systematic expansion methodology based on the Manhattan distance weighting. For the standard 3×3 kernel:

$$K_{3\times3} = \begin{bmatrix} 0 & 1 & 0 \\ 1 & -4 & 1 \\ 0 & 1 & 0 \end{bmatrix}\# \tag{14}$$

where $K_{3\times3}$ represents the 3×3 Laplacian kernel with elements arranged to approximate the discrete second-derivative operation. For 5×5 or larger kernels, weights are assigned according to the Manhattan distance d = $|i - c| + |j - c|$, where c is half the kernel size. The 5×5 kernel design exemplifies this approach.

$$K_{5\times5}(i,j) = \begin{cases} -20 & d = 0 \\ 4 & d = 1 \\ 1 & d = 2 \wedge |i-c| = |j-c| = 1 \\ 0 & \text{otherwise} \end{cases}\# \tag{15}$$

where $K_{5\times5}(i,j)$ represents the value of the 5×5 Laplacian kernel at position (i,j), d denotes the Manhattan distance from the center, and c is the center position index of the Laplacian kernel. All kernels maintain the zero-sum property essential for the Laplacian operation:

$$\sum_{i=0}^{size-1}\sum_{j=0}^{size-1} K_{\text{Laplace},k}(i,j) = 0\# \tag{16}$$

where the summation covers all kernel positions (i,j), the symbol *size* represents the Laplacian kernel size, and the zero result ensures that the kernels respond only to intensity variations in the image and produce zero response in regions of constant intensity, preventing unnecessary enhancement of homogeneous areas while amplifying variations associated with defects and structural features.

The relationship between the kernel size and spatial frequency response follows the approximate equation:

$$f_c \approx \frac{f_k}{size}\# \tag{17}$$

where f_c represents the cutoff frequency in cycles per pixel and f_k denotes a proportionality constant typically ranging from 0.6 to 0.8. This relationship reveals the fundamental connection between the kernel size and the spatial frequencies to which the kernel responds: smaller

kernels with higher cutoff frequencies capture finer details and sharper edges, whereas larger kernels with lower cutoff frequencies respond to broader features and more gradual intensity variations. This frequency-space interpretation provides a comprehensive framework for understanding how different kernel sizes capture distinct aspects of the image content, ensuring that defects of various scales, from microscopic cracks to larger structural anomalies, are appropriately detected and enhanced.

3.4 Method for Performing Pixel-Level Multiscale Adaptive Fusion

The pixel-level fusion process integrates enhanced representations from all scales through a weighted combination that adapts to the local detail characteristics. The enhancement at each individual scale follows the equation:

$$F_k(x,y) = (1 + \alpha_k(x,y))I_{\log}(x,y)\# \quad (18)$$

where $F_k(x,y)$ represents an enhanced image at scale k. This equation embodies the core enhancement mechanism at each scale, with the term $(1+\alpha_k(x,y))$ functioning as a spatially varying gain that amplifies or attenuates the pixel value based on the coefficient importance. When significant details are detected at a particular scale ($\alpha_k(x,y) > 0$), the pixel value is amplified, enhancing the visibility of these details. When no significant details are present ($\alpha_k(x,y) \le 0$), minimal or no enhancement is applied, preventing the artificial amplification of noise or irrelevant variations. This scale-specific approach enables the targeted enhancement of features based on their size characteristics, ensuring that small defects receive appropriate enhancement without adversely affecting larger structures.

Multiscale fusion combines all scales through equal-weight averaging as follows:

$$F_{\text{final}}(x,y) = \frac{1}{N}\sum_{k=1}^{N} F_k(x,y)\# \quad (19)$$

This equation can be algebraically expanded to reveal the underlying enhancement mechanism as follows:

$$F_{\text{final}}(x,y) = I_{\log}(x,y) + \frac{1}{N} I_{\log}(x,y)\sum_{k=1}^{N} \alpha_k(x,y)\# \quad (20)$$

where the expanded form clearly separates the original image content $I_{\log}(x,y)$ from the enhancement component $\frac{1}{N} I_{log}(x,y)\sum_{k=1}^{N} \alpha_k(x,y)$.

This separation has significant implications: the enhancement is proportional to both the local intensity value and the cumulative importance across all scales. Multiplication by $I_{\log}(x,y)$ ensures that the enhancement respects the local intensity context: brighter regions receive stronger absolute enhancement, whereas darker regions receive more modest enhancement, maintaining a natural appearance and preventing artificial-looking results. The summation over the importance coefficients ensures that the details detected at multiple scales contribute collectively to the final enhancement, providing comprehensive detail amplification across the entire spectrum of feature sizes present in the image.

3.5 Method for Reconstructing Enhanced DR Image

The final enhanced image requires transformation back to the conventional 16-bit grayscale representation to ensure compatibility with standard display systems and analysis tools. The method used to reconstruct the final enhanced DR Image is as follows:

$$I_{\text{enhanced}}(x,y) = \text{round}\left(65535\frac{F_{\text{final}}(x,y) - F_{\min}}{F_{\max} - F_{\min}}\right)\# \quad (21)$$

where $I_{\text{enhanced}}(x,y)$ represents the enhanced image pixel value in grayscale levels at position (x,y), round$(\cdot)$ signifies the rounding function to the nearest integer, $F_{\text{final}}(x,y)$ denotes the final fusion result, $F_{\min}=\min(F_{\text{final}})$ represents the minimum value of the fusion result across the entire image, $F_{\max}=\max(F_{\text{final}})$ indicates the maximum value of the fusion result across the entire image, and 65535 corresponds to the maximum value in the

65535 corresponds to the maximum value in the 16-bit representation.

This normalization process serves two crucial purposes in the enhancement pipeline: first, it maps the processed floating-point values back to the standard 16-bit integer format required for display, storage, and subsequent analysis; second, it preserves the relative contrast relationships established during the multiscale fusion. This mapping preserves the proportional differences between pixel values, ensuring both enhanced visibility of details and maintained fidelity of image intensity relationships. This preservation is crucial for quantitative analysis, where absolute or relative intensities have physical significance pertaining to material properties, thickness variations, or defect characteristics.

3.6 Gaussian Blurring Induced Detail Destruction and Avoidance Strategy

Traditional multiscale analysis methods employ Gaussian convolution for scale-space representation, with the convolution operation mathematically expressed as

$$I_{\text{smooth}}(x, y, \sigma) = I(x, y) * G(i, j, \sigma)\# \quad (22)$$

where $I_{\text{smooth}}(x,y,\sigma)$ represents the result of the smoothed image at scale σ and position (x,y), * denotes the convolution operation, and $G(i,j,\sigma)$ denotes the value of the Gaussian kernel at scale σ and position (i,j). The Gaussian kernel is defined as follows:

$$G(i, j, \sigma) = \frac{1}{2\pi\sigma^2} e^{-\frac{i^2+j^2}{2\sigma^2}}\# \quad (23)$$

where the term $1/(2\pi\sigma^2)$ serves as a normalization constant. The frequency response of this operation reveals its fundamental limitation:

$$\mathcal{F}\{G(i, j, \sigma)\} = e^{-2\pi^2\sigma^2(u^2+v^2)}\# \quad (24)$$

where $F\{\cdot\}$ denotes the Fourier transform, and (u,v) represents the spatial frequency coordinates. This exponential decay demonstrates that the Gaussian convolution systematically attenuates the high-frequency components in the image, with the degree of attenuation increasing with both the spatial frequency and scale parameter σ.

While this smoothing behavior is beneficial for noise reduction, it fundamentally damages the most critical information for industrial DR image enhancement: fine details, sharp edges, and high-frequency textures that correspond to defect signatures and material discontinuities. This creates an inherent trade-off in traditional approaches—the same operation that reduces noise also destroys important details, severely limiting the effectiveness for industrial inspection applications where preserving fine features is essential for reliable defect detection.

The proposed method addresses this limitation by eliminating Gaussian convolution operations and employing a three-pronged alternative strategy: (1) this comprehensive approach preserves the high-frequency components containing critical defect signatures while providing robust enhancement through complementary processing stages; (2) the logarithmic transformation handles dynamic range issues without spatial averaging, thereby maintaining finer detail integrity than Gaussian convolution; and (3) the direct multiscale Laplacian methodology extracts the information of details across the spatial frequencies without the blurring inherent using Gaussian operations. The adaptive fusion process achieves noise robustness through selective enhancement rather than spatial smoothing, representing a fundamentally different paradigm for handling image quality challenges while preserving the essential structural information.

IV. RESULTS

4.1 Experimental Setup

The experimental study employed DR images obtained from nondestructive welding quality inspections to comprehensively validate the proposed method. These DR images were sourced from nondestructive testing across three welding scenarios and were stored in DICOM format with a dynamic range of 0-65535.

To rigorously assess the efficacy of the proposed method, a comparative analysis was performed using several DR image detail-enhancement techniques. These benchmark methods included a method based on histogram equalization (HE)

[32], a method based on contrast-limited adaptive histogram equalization (CLAHE) [33], a method based on discrete wavelet transform (DWT) [34], and a CNN-based detail enhancement method (CNN-DEMD) [35]. It should be specifically noted that the dataset employed for training the CNN-DEMD benchmark comprised 1202 original DR images sourced from nondestructive testing results of weld quality. Following data augmentation, the dataset used to train the CNN-DEMD comprised 3606 samples.

The experiment utilized 30 DR images of weld nondestructive testing sourced from different industrial sectors (10 DR images from each sector) for comprehensive testing. All DR images were acquired using the system shown in Fig. 2. A brief summary of the 20 DR images is presented in Table 2.

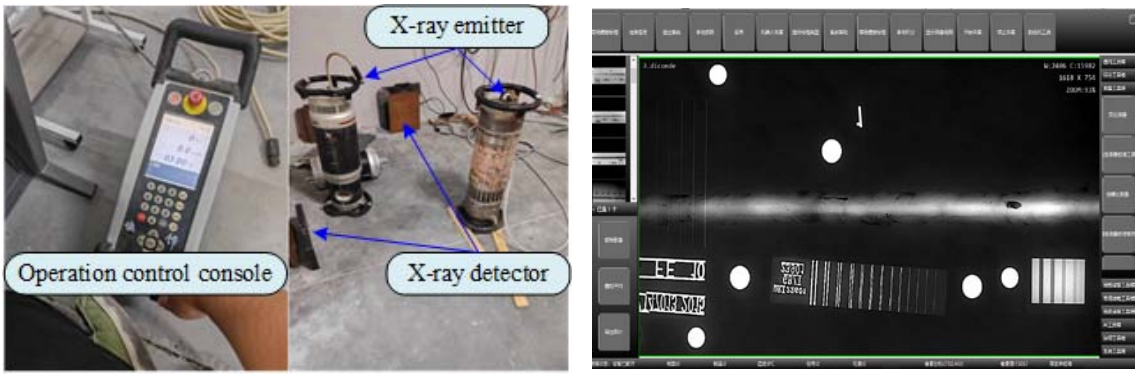

(a) (b)

Fig. 2: Experimental platform: (a) hardware and (b) software

Table 2: A Brief Summary of the 30 DR Images

Source	Resolution	Major Defects	Average Thickness/mm	Total
Weld in ship plate	2048 x 1800	Linear defects and pores	33	10
Weld in boiler	1820 x 768	Linear defects and pores	38	10
Weld in oil pipeline	1280 x 1024	Linear defects and pores	26	10

Three metrics were employed for the quantitative assessment of detail-enhancement performance. The Peak Signal-to-Noise Ratio (PSNR) functions as a statistical metric for evaluating the ratio between the maximum possible signal power and the power of the corrupting noise, and is commonly used for image quality assessment. The Structural Similarity Index Measure (SSIM) quantifies the perceived structural fidelity between a processed image and its original, unprocessed counterpart. The Spatial Frequency (SF), which indicates the overall activity level in an image, is used to measure the change rate of intensity across pixels. Elevated SF values are associated with sharper edge definitions and richer textural details, correlating with superior perceptual quality. The computations for PSNR, SSIM, and SF are defined by Equations (25), (26), and (27), respectively, as follows:

$$PSNR(\boldsymbol{E},\boldsymbol{S}) = 10\log_{10}\left\{\frac{65535^2}{\frac{\sum_{x=1}^{H}\sum_{y=1}^{W}[\boldsymbol{E}(x,y)-\boldsymbol{S}(x,y)]^2}{W\times H}}\right\}\# \tag{25}$$

$$SSIM(\boldsymbol{E},\boldsymbol{S}) = \frac{(2\mu_E\mu_S + c_1)(2\sigma_{ES} + c_2)}{(\mu_E{}^2 + \mu_S{}^2 + c_1)(\sigma_E{}^2 + \sigma_S{}^2 + c_2)}\# \tag{26}$$

$$\begin{cases} SF(\boldsymbol{E}) = \sqrt{H_G(\boldsymbol{E})^2 + V_G(\boldsymbol{E})^2} \\ H_G(\boldsymbol{E}) = \sqrt{\dfrac{1}{W \times H} \sum_{x=1}^{W} \sum_{y=1}^{H-1} [\boldsymbol{E}(x,y) - \boldsymbol{E}(x,y+1)]^2} \\ V_G(\boldsymbol{E}) = \sqrt{\dfrac{1}{W \times H} \sum_{x=1}^{W-1} \sum_{y=1}^{H} [\boldsymbol{E}(x,y) - \boldsymbol{E}(x+1,y)]^2} \end{cases} \#$$

where $PSNR(E,S)$ is the peak signal-to-noise ratio of the image E relative to the image S, $SSIM(E,S)$ is the structural similarity index measure of the image E relative to the image S, $SF(E)$ is the spatial frequency of the image E, $H_G(E)$ computes the horizontal gradient of the image E, $V_G(E)$ computes the vertical gradient of the image E, W is the image width, H is the image height, μ_E is the mean of the image E, c_1 and c_2 are two constants, μ_S is the mean of the image S, σ_E is the variance of the image $\boldsymbol{E}$, σ_S is the variance of the image S, and σ_{ES} is the covariance of the images $\boldsymbol{E}$ and S.

The parameter configuration for the proposed method utilized N=4 scales with kernel sizes progressively increasing from 3×3 to 9×9, enhancement factor λ=5N=20 controlling detail enhancement sensitivity, and logarithm base a=10 compressing the DR image grayscale. This parameter set was determined through systematic optimization of the experimental dataset to achieve a balanced performance across different image types and defect characteristics.

4.2 Objective Analysis

After applying several distinct methodologies for detail enhancement to the DR images obtained from three different sources, the processed results are presented in Figs. 3–5. It should be noted that the red-marked areas in these figures indicate defect regions. For reference, although the entire experiment comprised 30 images, only representative samples from each source are displayed here.

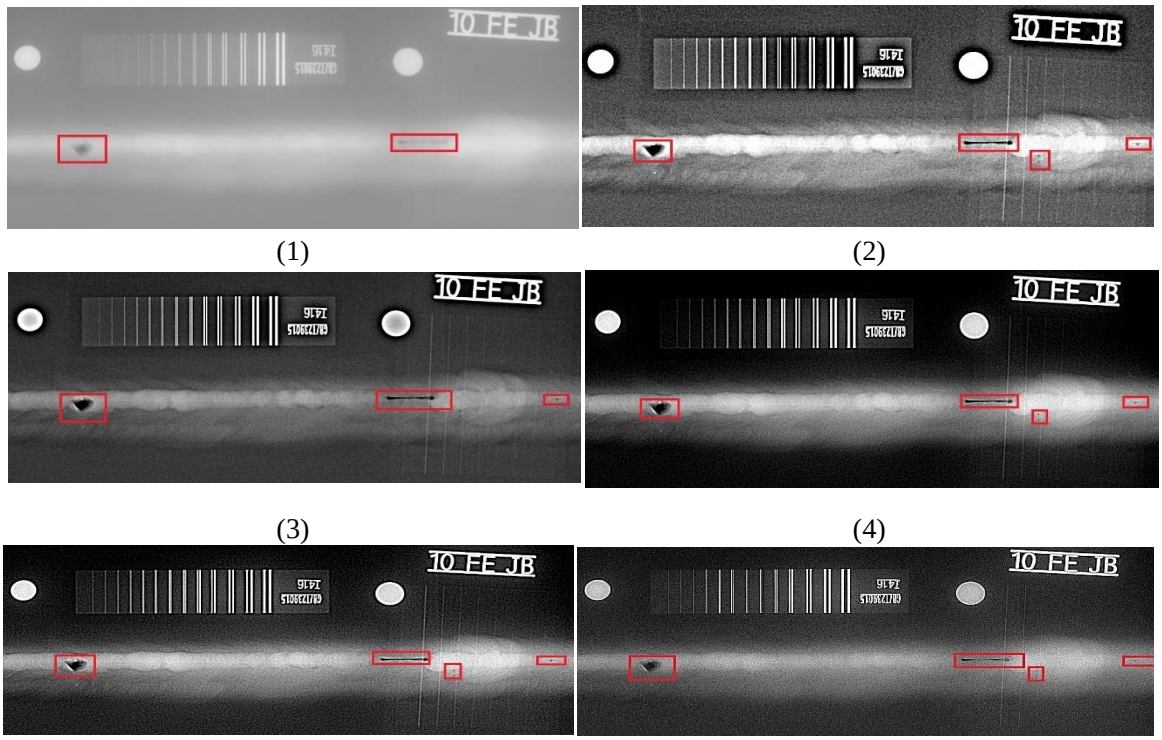

Fig. 3: Performance of different methods on a ship plate weld image: (1) original, (2) HE, (3) CLAHE, (4) DWT, (5) CNN-DEMD, and (6) proposed method

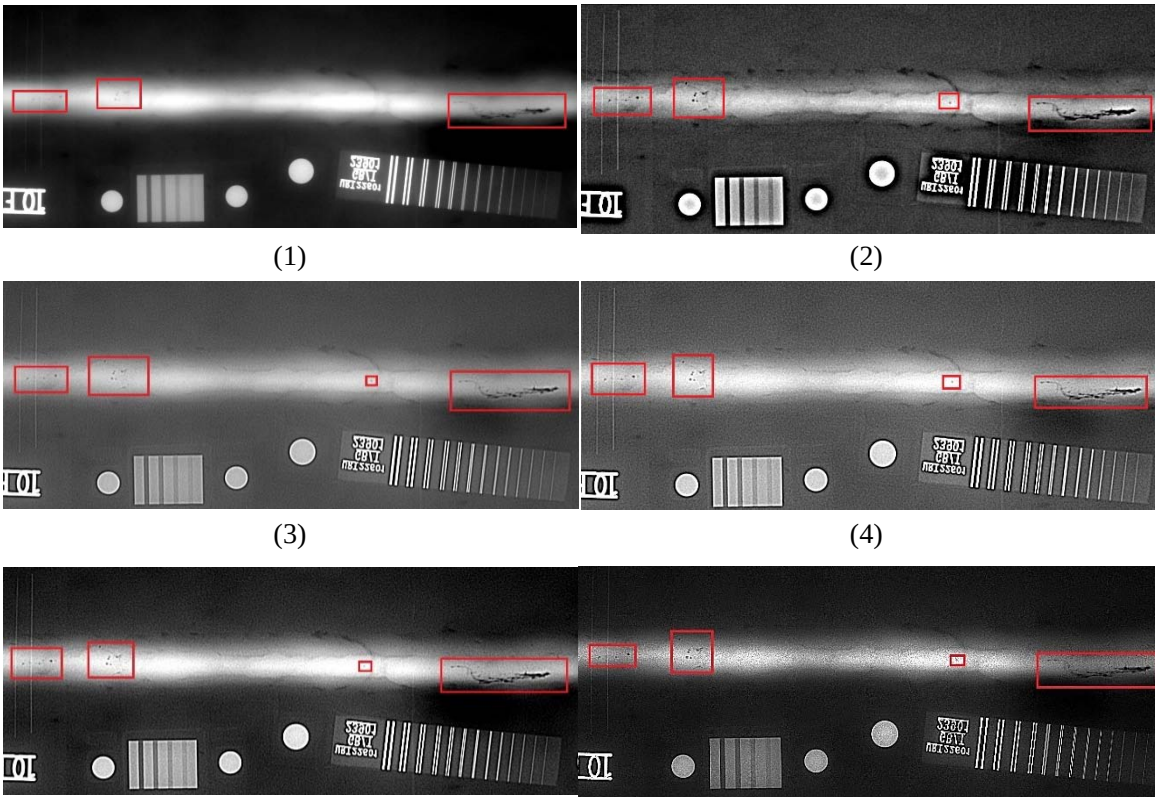

Fig. 4: Performance of proposed method against existing methods on a boiler weld image: (1) original, (2) HE, (3) CLAHE, (4) DWT, (5) CNN-DEMD, and (6) proposed method

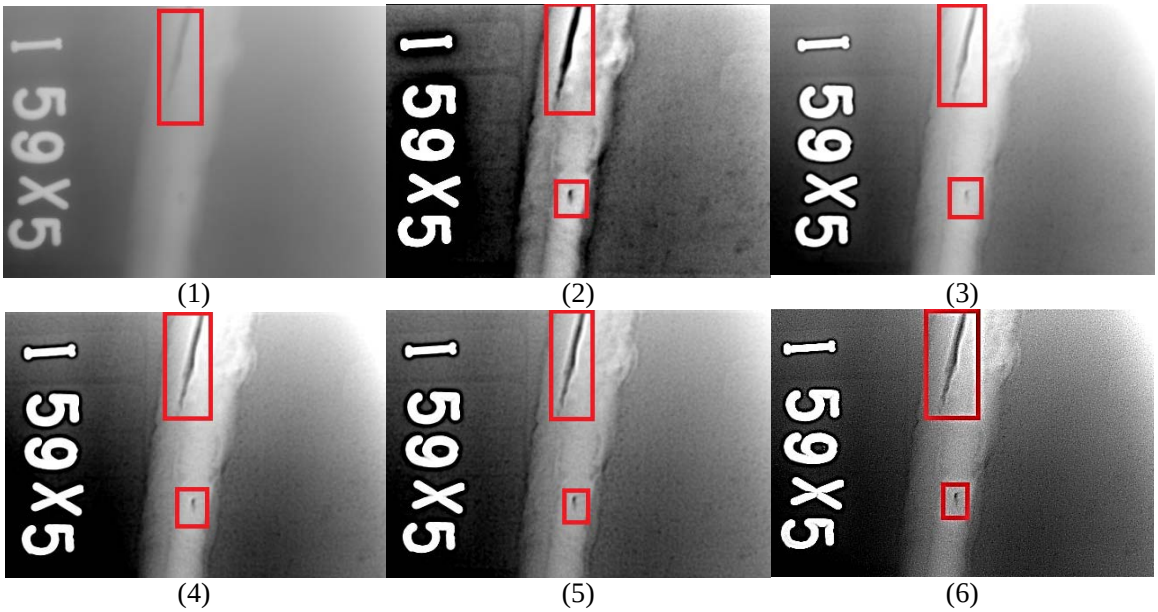

Fig. 5: Performance of the proposed method against existing algorithms on an oil-pipeline weld image: (1) original, (2) HE, (3) CLAHE, (4) DWT, (5) CNN-DEMD, and (6) proposed method

A visual examination of Figs. 2–4 reveals that the proposed method achieves superior performance compared with other algorithms, exhibiting enhanced clarity, sharpness, fidelity, delicacy, and artifact reduction compared with other algorithms. This method effectively enhances images via pixel-level adaptive fusion, leveraging logarithmic transformation and a multiscale Laplacian transform.

4.3 Result Analysis

Notably, the proposed method achieved superior performance, attaining the highest mean PSNR across all three industrial weld inspection scenarios—ship plates, boilers, and oil pipelines—with values of 26.12, 25.17, and 26.96, respectively (Table 3). This reflects a statistically significant and consistent enhancement over existing techniques.

As illustrated in Table 3, performance escalates progressively from conventional approaches such as HE and CLAHE (PSNR: 11–15), through moderate gains with DWT (~17–20), to a marked improvement via CNN-DEMD (23–26). The proposed method builds upon this trajectory, delivering further gains.

Moreover, the proposed approach demonstrates enhanced statistical robustness, exhibiting the lowest standard deviation in PSNR across test cases (0.68, 0.74, 0.71), as shown in Table 4. This trend of declining variability—from traditional to advanced techniques—culminates in the proposed method, underscoring its stability and reliability.

Table 3: Average PSNR Across Different Enhancement Methods

DR Image Source	HE	CLAHE	DWT	CNN-DEMD	Proposed Method
Weld in ship plate	13.68	14.29	19.33	24.89	26.12
Weld in boiler	12.86	14.35	17.87	23.38	25.17
Weld in oil pipeline	11.53	15.18	20.12	25.57	26.96

Table 4: Standard Deviation of PSNR across different enhancement methods

DR Image Source	HE	CLAHE	DWT	CNN-DEMD	Proposed Method
Weld in ship plate	1.53	1.37	1.15	0.82	0.68
Weld in boiler	1.68	1.42	1.23	0.87	0.74
Weld in oil pipeline	1.71	1.29	1.08	0.93	0.71

A comparative analysis of the experimental results (Tables 5 and 6) demonstrates the consistent superiority of the proposed method in terms of structural fidelity and robustness across all test scenarios. As indicated in Table 5, the proposed technique attained the highest mean Structural Similarity Index Measure (SSIM) for welds from ship plates (0.75), boilers (0.73), and oil pipelines (0.76), reflecting more effective structural preservation relative to the benchmark approaches. The performance hierarchy remains stable: the proposed method surpasses CNN-DEMD, which in turn exceeds the Discrete Wavelet Transform (DWT) method, whereas conventional techniques such as Histogram Equalization (HE) and CLAHE yield markedly lower SSIM values.

This performance advantage is complemented by enhanced robustness, quantified by the SSIM standard deviations in Table 6. For the challenging "Weld in ship plate" dataset, the proposed method achieved the highest mean SSIM and the lowest deviation (0.062), indicating superior stability. A comparable trend was observed for the boiler welds. Although the deviation for oil pipeline welds (0.069) slightly exceeded that of the DWT method (0.061), this marginal trade-off was substantially offset by a significant advantage in the mean SSIM (0.76 vs. 0.61). Collectively, the high mean SSIM and generally low variance underscore the efficacy and reliability of the proposed method in delivering structurally faithful enhancements across various industrial radiography contexts.

Table 5: Average SSIM across different enhancement methods

DR Image Source	HE	CLAHE	DWT	CNN-DEMD	Proposed method
Weld in ship plate	0.33	0.47	0.68	0.72	0.75
Weld in boiler	0.42	0.56	0.63	0.68	0.73
Weld in oil pipeline	0.38	0.49	0.61	0.73	0.76

Table 6: Standard Deviation of SSIM across different enhancement methods

DR Image Source	HE	CLAHE	DWT	CNN-DEMD	Proposed method
Weld in ship plate	0.084	0.081	0.076	0.072	0.062
Weld in boiler	0.075	0.077	0.069	0.069	0.067
Weld in oil pipeline	0.073	0.068	0.061	0.064	0.069

As shown in Table 7, the proposed image enhancement method consistently achieved the highest average Spatial Frequency (SF) across all three industrial weld inspection scenarios. For welds in ship plates, boilers, and oil pipelines, SF values of 18.86, 18.27, and 19.18 were attained, respectively, indicating superior image clarity and textural enhancement. A clear performance hierarchy is observable: conventional techniques like HE and CLAHE yield the lowest SF values (9.84-13.76), followed by a moderate improvement with DWT (14.82-15.26). A significant leap is realized by the CNN-DEMD method (17.33-18.42), which the proposed method subsequently surpasses.

The superior performance of the proposed method is coupled with its exceptional stability. The standard deviation data presented in Table 8 consistently demonstrate the lowest or nearly lowest variance in the SF output. With standard deviations of 0.24, 0.21, and 0.23 for the respective test cases, the method exhibited remarkable robustness. This trend of decreasing standard deviation from traditional to advanced methods culminates in the proposed algorithm, confirming its reliability in minimizing performance fluctuations while maximizing spatial frequency.

Table 7: Average SF across different enhancement methods

DR Image Source	HE	CLAHE	DWT	CNN-DEMD	Proposed method
Weld in ship plate	10.15	12.15	15.14	18.19	18.86
Weld in boiler	9.84	11.83	15.26	17.33	18.27
Weld in oil pipeline	11.33	13.76	14.82	18.42	19.18

Table 8: Standard Deviation of SF across different enhancement methods

DR Image Source	HE	CLAHE	DWT	CNN-DEMD	Proposed method
Weld in ship plate	0.53	0.43	0.33	0.23	0.24
Weld in boiler	0.55	0.41	0.31	0.26	0.21
Weld in oil pipeline	0.52	0.44	0.32	0.22	0.23

As quantified in Table 9, the proposed method yields substantial PSNR enhancements across all benchmarked image-enhancement techniques in three welding inspection scenarios. Two principal findings emerged: first, traditional methods, notably HE and CLAHE, exhibited the most marked relative gains, with PSNR increases exceeding 75% and, in one case, surpassing 130%, underscoring a pronounced performance gap relative to the proposed technique. Second, and more significantly, the method demonstrates universal applicability, consistently refining even advanced approaches, such as CNN-DEMD. The modest yet consistent gains (approximately 4–8%) observed here are paradoxically indicative of CNN-DEMD's strong baseline performance, thereby highlighting the proposed method's efficacy as a robust post-processing or integration module. In summary, the results systematically affirm the method's capacity to markedly augment conventional algorithms while delivering measurable improvements to the state-of-the-art deep learning models.

Table 9: The proposed method's enhancement of the PSNR for other methods

Compared Method	Weld in Ship Plate /%	Weld in Boiler /%	Weld in Oil Pipeline /%
HE	90.94	95.72	133.82
CLAHE	82.79	75.40	77.60
DWT	35.13	40.85	34.00
CNN-DEMD	4.94	7.66	5.44

As evidenced by the SSIM enhancement metrics in Table 10, the proposed method consistently improves the structural similarity across a spectrum of benchmark techniques, following a distinct and interpretable trend. The most pronounced gains were observed with traditional algorithms: HE achieved a remarkable 127.27% improvement in "Weld in ship plate" and 100.00% in "Weld in oil pipeline," culminating in a total improvement of 100.36%, whereas CLAHE exhibited a 48.34% total gain. These results indicate a strong compensatory effect on the structural distortions inherent to conventional approaches.

In contrast, enhancements for advanced methods, such as DWT and CNN-DEMD, although consistent, were more moderate (16.92% and 5.21%, respectively). This inverse correlation between methodological sophistication and improvement magnitude underscores the proposed method's capacity to deliver substantial benefits for weaker algorithms while still providing statistically meaningful refinements to the state-of-the-art techniques.

In summary, the consistent positive improvements validate the robustness and general applicability of the proposed method as a universal enhancer of structural fidelity in welding inspection imagery.

Table 10: The proposed method's enhancement of the SSIM for other methods

Compared Method	Weld in Ship Plate /%	Weld in Boiler /%	Weld in Oil Pipeline /%
HE	127.27	73.81	100.00
CLAHE	59.57	30.36	55.10
DWT	10.29	15.87	24.59
CNN-DEMD	4.17	7.35	4.11

As demonstrated in Table 11, the proposed method significantly enhanced the performance of various techniques across multiple welding inspection scenarios. Notably, the most substantial improvement was observed for the HE method, with a total improvement of 80.26%, reflecting considerable gains in weld detection accuracy for ship plates (85.81%), boilers (85.67%), and oil pipelines (69.29%).

Conversely, CLAHE exhibited moderate enhancement, achieving a 49.69% overall improvement, although its absolute performance remained lower, particularly in oil pipeline contexts (39.39%). The DWT-based method showed more limited gains, with a total improvement of 24.57%, whereas CNN-DEMD demonstrated the least improvement (4.41%), indicating its inherent robustness and lower susceptibility to further enhancement under the proposed framework.

These results collectively underscore the versatility and efficacy of the proposed method in augmenting both traditional and advanced techniques, with the degree of improvement being inversely related to the baseline sophistication of each compared method.

Table 11: The proposed method's enhancement of the SF for other methods

Compared Method	Weld in Ship Plate /%	Weld in Boiler /%	Weld in Oil Pipeline /%
HE	85.81	85.67	69.29
CLAHE	55.23	54.44	39.39
DWT	24.57	19.72	29.42
CNN-DEMD	3.68	5.42	4.13

V. DISCUSSION

A Gaussian-free multiscale detail-enhancement framework is proposed for industrial DR images that fundamentally addresses the inherent limitation of detail destruction in conventional approaches using Gaussian convolution. The core innovation lies in the integration of logarithmic transformation with direct multiscale Laplacian analysis, the development of adaptive importance coefficients using hyperbolic tangent functions, a systematic methodology for generating Laplacian kernels, and achieving multiscale pixel-level adaptive fusion. Collectively, these elements establish a rigorous and mathematically coherent framework for detail-preserving DR-image-detail enhancement.

The experimental results demonstrate the efficacy and general applicability of our method. The proposed framework universally enhances the established techniques—HE, CLAHE, DWT, and CNN-DEMD—across diverse industrial weld inspection scenarios (ship plate, boiler, and oil pipeline). Most strikingly, it elevates the PSNR of HE by 133.82% for the oil pipeline welds. Substantial gains were also observed in the SSIM (HE improved by 127.27% for ship plate welds) and SF (HE enhanced by 85.81% for the same application). Although the performance uplift over more sophisticated methods, such as CNN-DEMD, is more modest (e.g., 4.94–7.66% for PSNR), the consistent positive enhancement across all benchmarks underscores its robustness as a superior preprocessing or integrated solution for nondestructive testing.

The significant results achieved through experimental validation include demonstrated superiority in micron-scale defect detection, robust performance across diverse industrial applications and image characteristics, and practical implementation feasibility for real-time inspection systems. The method's ability to enhance detail visibility while preserving structural integrity addresses a critical need in industrial nondestructive testing, where reliable defect detection must be balanced with maintaining an accurate structural representation for subsequent analysis and decision-making.

This study had several limitations that warrant consideration. First, the proposed framework was developed and validated specifically on DR images of weld defects; its efficacy on DR images from other industrial sources (e.g., castings or composite materials) remains unverified. Second, despite its performance gains, the computational complexity of the multiscale analysis requires further optimization for real-time deployment in resource-constrained environments. Finally, the experimental validation, while demonstrating robust results, was conducted on a limited dataset, and large-scale comprehensive testing is required to fully ascertain its generalizability.

Future research should prioritize three principal avenues of investigation. First, efforts should be directed toward broadening the scope of application of the method to encompass a wider array of industrial nondestructive testing (NDT) scenarios, with a rigorous assessment of its cross-domain robustness. Concurrently, dedicated efforts will be channeled into algorithmic refinement and implementation optimization to improve the computational efficiency. Furthermore, a more comprehensive evaluation using large-scale, multi-source datasets will be undertaken to thoroughly validate the performance of the proposed method. This may be supplemented by the development of adaptive parameter strategies and their integration with deep learning models to augment feature learning capabilities.

VI. CONCLUSION

To address the limitations inherent in existing detail-enhancement techniques for industrial DR images, this study introduces a novel Gaussian-free detail-enhancement framework by integrating logarithmic transformation and multiscale Laplacian analysis. This method fundamentally departs from traditional Gaussian-based approaches by eliminating the blur-inducing convolution operations. This study establishes a new detail-enhancement paradigm for industrial DR images through a multiscale, pixel-level adaptive fusion mechanism that directly and faithfully preserves critical image details.

The superior performance and generalizability of the framework were demonstrated through rigorous quantitative evaluations. It achieves unprecedented enhancement across diverse weld inspection scenarios, elevating the PSNR of a basic HE method by 133.82% for oil pipeline-welds. Substantial gains in the SSIM (up to 127.27%) and SF (up to 85.81%) further confirmed its efficacy. Critically, it delivers consistent, albeit more modest, improvements over sophisticated benchmarks such as CLAHE, DWT, and CNN-DEMD, underscoring its robustness as a premier preprocessing or integrated solution for nondestructive testing.

This study makes three pivotal contributions: (1) it provides a highly effective technical foundation with significant potential to transform quality assurance in manufacturing; (2) it inaugurates a Gaussian-free paradigm that prioritizes structural fidelity, which is a critical requirement for high-precision industrial applications; and (3) it provides an adaptive pixel-level fusion technology with precise control mechanisms for defect-specific enhancements.

ACKNOWLEDGEMENT

This study was funded by the Guangxi Science and Technology Program, China (Grant No. 2025LTLT02001).

REFERENCES

1. Grigorchenko, S.A. and V.I. Kapustin, *Enhancing the Efficiency of Defect Image Identification in Computer Decoding of Digital Radiographic Images of Welded Joints in Hazardous Industrial Facilities*. Russian Journal of Nondestructive Testing, 2024, 60(12): 1387-1395. https://www.doi.org/10.1134/s1061830924602836.
2. Kenderian, S., et al., *Contrast-based notch-to-crack transfer function for digital radiography*. Insight, 2024, 66(7): 400-408. https://www.doi.org/10.1784/insi.2024.66.7.400.
3. Xue, W.J., Y.M. Wang, and Z. Qin, *Multiscale Feature Attention Module Based Pyramid Network for Medical Digital Radiography*

Image Enhancement. Ieee Access, 2024, 12: 53686-53697. https://www.doi.org/10.1109/access.2024.3387413.
4. Yoo, S., et al., *Analysis of absorption signal and noise in thin phosphor detectors for high-energy transmission radiography*. Journal of Instrumentation, 2023, 18(10). https://www.doi.org/10.1088/1748-0221/18/10/c10017.
5. García-Pérez, A., M.J. Gómez-Silva, and A. de la Escalera-hueso, *Improving automatic defect recognition on GDXRay castings dataset by introducing GenAI synthetic training data*. Ndt & E International, 2025, 151. https://www.doi.org/10.1016/j.ndteint.2024.103303.
6. Ma, M.L., et al., *Nondestructive classification of internal defects in camellia seeds and chestnuts using X-ray imaging: optimization and comparison of deep learning classifiers*. Food Control, 2025, 176. https://www.doi.org/10.1016/j.foodcont.2025.111367.
7. 7. Wilson, F., et al., *An Analysis of Input Parameters for Film-Based Flash X-Ray Radiography*. Experimental Techniques, 2025. https://www.doi.org/10.1007/s40799-025-00836-y.
8. Sun, S.L., et al., *Tibia-YOLO: An Assisted Detection System Combined with Industrial CT Equipment for Leg Diseases in Broilers*. Applied Sciences-Basel, 2024, 14(3). https://www.doi.org/10.3390/app14031005.
9. Zhang, H.X., et al., *Industrial digital radiographic image denoising based on improved KBNet*. Journal of X-Ray Science and Technology, 2024, 32(6): 1521-1534. https://www.doi.org/10.3233/xst-240125.
10. Son, J. and J. Park, *Recent Trends in Computed Tomography(CT) in Industry*. Journal of the Korean Society for Nondestructive Testing, 2023, 43(5): 417-430. https://www.doi.org/10.7779/jksnt.2023.43.5.417.
11. Wang, Z.B., et al., *Underwater Image Enhancement via Adaptive Color Correction and Stationary Wavelet Detail Enhancement*. Ieee Access, 2024, 12: 11066-11082. https://www.doi.org/10.1109/access.2024.3354169.
12. Zhang, X.Y., et al. *A Wavelet-based Diffusion Model for Low-light Image Enhancement in Raw Space*. in *16th International Conference on Graphics and Image Processing-ICGIP-Annual*. 2024. Nanjing University of Science and Technology School of Computer Science an, Nanjing, PEOPLES R CHINA. https://www.doi.org/10.1117/12.3057717.
13. Ai, X., G.X. Ni, and T.Y. Zeng, *A sharpening median filter for Cauchy noise with wavelet based regularization*. Journal of Computational and Applied Mathematics, 2025, 467. https://www.doi.org/10.1016/j.cam.2025.116625.
14. Zhang, F.F., et al., *Brightness segmentation-based plateau histogram equalization algorithm for displaying high dynamic range infrared images*. Infrared Physics & Technology 2023. 134. https://www.doi.org/10.1016/j.infrared.2023.104894.
15. Kong, T.R., W.P. Rey and M. Assoc Computing. *Self-supervised Low-light Image Enhancement Based on Retinex and Histogram Equalization Prior*. in *1st International Conference on Image Processing Machine Learning and Pattern Recognition*. 2024. Guangzhou, PEOPLES R CHINA. https://www.doi.org/10.1145/3700906.3700929.
16. Du, Z.M., H.A. Li, and F.L. Han, *Dynamic Fusion for Generating High-Quality Labels in Low-Light Image Enhancement*. IEEE Signal Processing Letters, 2025, 32: 2324-2328. https://www.doi.org/10.1109/lsp.2025.3575608.
17. Xiang, Y.J. and G.S. Hu. *SFT-Net: low-light image enhancement network based on spatial feature transformation*. in *2025 International Conference on Remote Sensing, Mapping, and Image Processing-RSMIP*. 2025. Sanya, PEOPLES R CHINA. https://www.doi.org/10.1117/12.3067585.
18. Zhou, L.Q., et al., *WDFN: Wavelet-Based Decomposition-Fusion Network for Low-Light Underwater Image Enhancement*. IEEE Transactions on Geoscience and Remote Sensing, 2025. 63. https://www.doi.org/10.1109/tgrs.2025.3578662.

19. Dennison, M., et al., *Image Quality Indicator Localization Using Mask R-Cnn*. Materials Evaluation 2025. 83(3).
20. Liang, Z.H., X.Y. Wu, and W. Wu, *Latent Space Diffusion Model Digital Radiography Image Super-Resolution Enhancement Algorithm*. Laser & Optoelectronics Progress, 2025, 62(16). https://www.doi.org/10.3788/lop250503.
21. Hena, B., et al., *Towards Enhancing Automated Defect Recognition (ADR) in Digital X-ray Radiography Applications: Synthesizing Training Data through X-ray Intensity Distribution Modeling for Deep Learning Algorithms*. Information, 2024, 15(1). https://www.doi.org/10.3390/info15010016.
22. Aytekin, E.K., M. Dikmen, and Ieee. *An Approach with Effective Guided Filter and Lipschitz Constraint Based CLAHE for Improving X-Ray Image Details*. in *7th International Congress on Human-Computer Interaction, Optimization and Robotic Applications-ICHORA*, 2025, Ankara, TURKIYE. https://www.doi.org/10.1109/ichora65333.2025.11017217.
23. Azad, R., et al. *Laplacian-Former: Overcoming the Limitations of Vision Transformers in Local Texture Detection*. in *26th International Conference on Medical Image Computing and Computer-Assisted Intervention (MICCAI)*, 2023, Vancouver, CANADA. https://www.doi.org/10.1007/978-3-031-43898-1_70.
24. Pal, M., et al., *A novel parallel mammogram sharpening framework using modified Laplacian filter for lumps identification on GPU*. Innovations in Systems and Software Engineering, 2024. 20(3): p. 329-345. https://www.doi.org/10.1007/s11334-024-00562-5.
25. Sari, I.N. and W.W. Du, *Weighted Similarity-Confidence Laplacian Synthesis for High-Resolution Art Painting Completion*. Applied Sciences-Basel, 2024, 14(6). https://www.doi.org/10.3390/app14062397.
26. Lin, J.C., et al., *DdeNet: A dual-domain end-to-end network combining Pale-T ransformer and Laplacian convolution for sparse view CT reconstruction*. Biomedical Signal Processing and Control 2024. 96. https://www.doi.org/10.1016/j.bspc.2024.106593.
27. Liu, Z.B., et al., *Low-light image enhancement via multistage Laplacian feature fusion*. Journal of Electronic Imaging, 2024, 33(2). https://www.doi.org/10.1117/1.Jei.33.2.023020.
28. Yuan, S.Z., et al., *Quantum image edge detection based on Laplacian of Gaussian operator*. Quantum Information Processing 2024, 23(5). https://www.doi.org/10.1007/s11128-024-04392-z.
29. Zhao, K.H., et al., *Hyper-Laplacian Prior for Remote Sensing Image Super-Resolution*. IEEE Transactions on Geoscience and Remote Sensing, 2024. 62. https://www.doi.org/10.1109/tgrs.2024.3434998.
30. Shi, Y., et al. *Study On Industrial Computed Tomography Detection And Identification Of Inclusion Defects In Thick-Wall Polyethylene Pipe Butt Fusion Joint Within Nuclear Power Plant*. in *2024 Pressure Vessels and Piping Conference*. 2024. Bellevue, WA.
31. Iuso, D., et al., *PACS: Projection-driven with Adaptive CADs X-ray Scatter compensation for additive manufacturing inspection*. Precision Engineering-Journal of the International Societies for Precision Engineering and Nanotechnology, 2024. 90: p. 108-121. https://www.doi.org/10.1016/j.precisioneng.2024.08.006.
32. Mulyana D., et al., *Application of Gaussian Filter and Histogram Equalization for Repair x-ray Image*. Digital Zone: Jurnal Teknologi Informasi Dan Komunikasi, 2022, 13(1): 34-43. https://doi.org/10.31849/digitalzone.v13i1.9770.
33. Sun, A, et al, *Welding Image Enhancement Based on CLAHE and Guided Filter*. 2024 10th International Conference on Electrical Engineering, Control, and Robotics (EECR), Guangzhou, China, 2024: 285–290. https://doi.org/10.1109/EECR60807.2024.10607276.
34. Rajeswari, P., et al, *Denoising X-Ray Image Using Discrete Wavelet Transform and Thresholding*. In: Sivasubramanian, A., Shastry, P.N., Hong, P.C. (eds) Futuristic Communication and Network Technologies.

VICFCNT 2020. Lecture Notes in Electrical Engineering, 2022, 792, Springer, Singapore. https://doi.org/10.1007/978-981-16-4625-6_19.

35. Madmad, T., et al., *CNN-based morphological decomposition of X-ray images for details and defects contrast enhancement*. 2021 IEEE/CVF Conference on Computer Vision and Pattern Recognition Workshops (CVPRW), Nashville, TN, USA, 2021: 2170–2180. https://doi.org/10.1109/CVPRW53098.2021.00246.